Renewable Energy 222 (2024) 119825

Contents lists available at ScienceDirect

Renewable Energy

journal homepage: www.elsevier.com/locate/renene

Optimal array arrangement of oscillating wave surge converters: An analysis based on three devices☆

Daniela Benites-Munoz [a,b], Luofeng Huang [c,*], Giles Thomas [a]

[a] Department of Mechanical Engineering, University College London, London, UK
[b] Facultad de Ingeniería Marítima y Ciencias del Mar, Escuela Superior Politécnica del Litoral, Guayaquil, Ecuador
[c] School of Water, Energy and Environment, Cranfield University, Cranfield, UK

ARTICLE INFO

Keywords:
Wave farm
Oscillating wave surge converter
Array arrangement
Computational fluid dynamics
Reactive power take-off
OpenFOAM

ABSTRACT

Wave farms consist of arrays of wave energy converters. However, ocean waves perturbed by one device will interact with its neighbouring devices, which can lead to more or less power yielded than operating the devices in isolation. Therefore, it is of significant interest to study the optimal layout and spacing to deploy multiple devices. In this work, a validated high-fidelity computational approach is used to study the optimal arrays of three oscillating wave surge converters by systematically varying the array arrangement in different wave conditions. The simulations demonstrate the wave interaction with multiple dynamic bodies and how this affects the overall power output. Furthermore, novel empirical rules are derived to design the optimal constructive layout for three devices in a given wave condition, and this can be extended to cases of numerous devices.

1. Introduction

The path towards commercialisation of a Wave Energy Converter (WEC) technology involves increasing the overall energy efficiency whilst decreasing the operational and maintenance costs [1]. Wave farms can contribute to this goal by utilising premium wave resources, saving electrical components, and integrated management [2,3]. Nonetheless, designing the layout of numerous devices within a wave farm is not a straightforward task. This is due to WEC interaction with their surrounding wavefield, making neighbouring devices' performance considerably different than operating in isolation. If designed properly, this neighbouring effect can be constructive, thus it is significant to accurately predict and utilise the wave interaction with multiple structures of a wave farm [4].

Among all the feasible WEC devices developed so far, the Oscillatory Wave Surge Converters (OWSCs) can convert wave motions into a structural rotation, such as the Oyster and the WaveRoller shown in Fig. 1. The OWSC devices are a promising solution since they can operate under a large variety of wave conditions [5,6], and this type of WEC does not require to be tuned in resonance with the incident wave field to achieve considerable estimates of the power capture width, which is the case of most other WECs [7]. Moreover, their geometry and operational mechanism lead to a large amount of hydrodynamic power being harnessed, thus considered one of the most efficient in terms of their annual energy absorption estimates [5,6,8].

To understand the hydrodynamic response of OWSC-array configurations, previous studies used semi-analytical models based on linear inviscid potential theory for small-amplitude oscillations, such as [10–13]. In Renzi and Dias [10] and Renzi et al. [13], it was found that a crucial parameter is the lateral spacing since it influences the maximum energy captured by forcing near-resonant behaviour and trapping the energy between devices. Recent studies, such as Noad and Porter [11] and Sarkar et al. [14,15] focused on finding optimum configurations using a semi-analytical approach. These studies seem to offer contradictory outcomes about the recommended separating distance and wave farm layout. Whilst for the former, staggered configurations enhance the performance of 3- and 5-OWSC arrays, for the latter [14] the in-line arrangement is sufficient to produce a strong interaction between the OWSCs. It is worth noting that the in-line configuration was reported in Cameron et al. [16] as the one used by the second-generation Oyster device, an OWSC-type WEC, as a starting point towards array extension.

While the above researches used linear-based solutions, the flap-type wave-structure interactions consist of strong nonlinearities. To

☆ The first author acknowledges her PhD scholarship provided by the Ecuadorian National Secretary of Higher Education, Science, Technology and Innovation (SENESCYT) and the Escuela Superior Politécnica del Litoral (ESPOL). The second author acknowledges grants received from Innovate UK (No. 10048187, 10079774, 10081314) and the Royal Society (IEC\NSFC\223253, RG\R2\232462).

* Corresponding author.
E-mail addresses: Daniela.benites.16@ucl.ac.uk (D. Benites-Munoz), luofeng.huang@cranfield.ac.uk (L. Huang), Giles.thomas@ucl.ac.uk (G. Thomas).

https://doi.org/10.1016/j.renene.2023.119825
Received 21 July 2023; Received in revised form 29 November 2023; Accepted 14 December 2023
Available online 18 December 2023

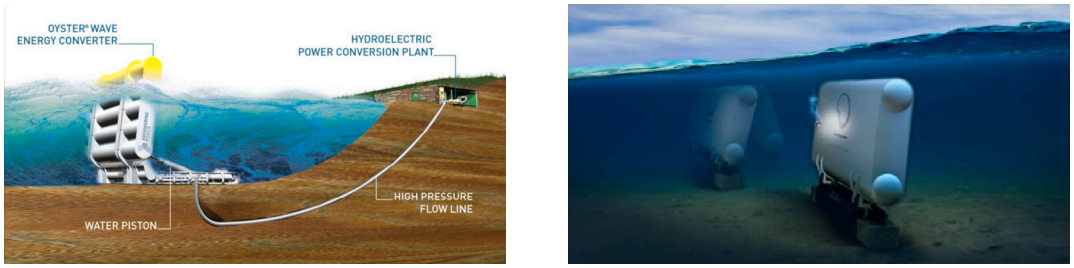

(a) Illustration of the Oyster

(b) Illustration of the WaveRoller

Fig. 1. Oscillating wave surge converters: surface-piercing and submerged types [9].

address this, the Computational Fluid Dynamics (CFD) technology including Smoothed-Particle Hydrodynamics (SPH) and Finite Volume Method (FVM) have been applied to OWSCs. The wave-structure interaction of OWSC devices has been addressed using the SPH method in [17,18]. The results obtained in [17] are specifically for a 2D and 3D OWSC device, and they were compared with previous experimental tests. The reported results showed that the simulations do not agree sufficiently with the experiments in the low pressure values. In [18], the SPH results were validated against experimental tests, and the influences of the Power Take-Off (PTO) and mass inertia of the device were further investigated. Yet, the approach using SPH is computationally expensive thus its further application for wave farms is limited due to the requirement of a larger computational domain, multiple structures and many more parameters [19]. For the cases using the FVM approach, studies of the hydrodynamic response of OWSC to ocean waves have been carried out by using the open-source software OpenFOAM. Benites-Munoz et al. [20–22] investigated the wave-structure interaction of a single OWSC device and validated the model against experiments. In particular, they investigated different types of Power Take-Off strategies and coupled their modelling with CFD, noting that PTO is not investigated in most contemporary CFD work on WECs [23]. It was found that, with the PTO taken into consideration, the curve of power capture as a function of the incident wavelength will reveal an optimal value, which does not show for the cases without PTO.

The application of Froude scaling for oscillating wave surge converters was investigated by [24,25] by assuming that the viscous forces are negligible. In both studies it is found that the numerical methods applied for the full-scale and models showed relatively accurate results for models of 1:40 scale or above. When using models of a larger scale, vortex effects besides the flap are thought to cause a reduction in the rotation amplitude of the device.

In summary, the wave-structure interaction of OWSC is considerably nonlinear, while previous CFD work that considered fully nonlinearities has focused on one single device due to computational costs and the high simulation difficulty level for multiple devices. It still remains a research gap to investigate the optimal array arrangement of OWSCs by CFD, thus facilitating its development in the form of wave farms.

In this context, the present paper aims to find the most advantageous layouts for a three-OWSC array operating under common sea conditions by finding the most compact design that allows the system to benefit from the associated increase in energy efficiency. This results from the devices within the wave farm interacting with each other through the sea environment where they are located. Alongside the arrangements, this study also focuses on the longitudinal and lateral spacings between the devices. Moreover, it contrasts the computational results estimated with those obtained using semi-analytical solutions from previous studies. Finally, it provides a set of parameters recommended for different layouts, highlighting the condition where the OWSC array will achieve the highest enhancement.

2. Computational approach

2.1. Simulation model

The open-source CFD code OpenFOAM [26,27] was used to establish a three-dimensional Numerical Wave Tank (NWT) and perform simulations in this work, as illustrated in Fig. 2. The NWT's (x, y) plane parallels the undistributed water surface, and the z-axis is positive upwards. Its dimensions are 16.00 m × 5.65–11.25 m × 0.60 m, corresponding to the length, width, and height; the width was varied depending on the lateral spacings between the devices. An array of three OWSC devices was located within the NWT. Each WEC is identical, and the dimensions were 0.024 m × 0.65 m × 0.34 m, corresponding to the thickness, width and height. The physical properties of the WEC included a mass of 5.97 kg and a moment of inertia of 0.091 kg m^2. The hinge of each device was located at 0.12 m measured from the sea bottom. A no-slip wall condition was applied to the bottom boundary $z = 0$ to model the presence of the seabed, and a static pressure condition was defined to the top boundary to account for the atmosphere. The domain was filled with water to a depth of 0.34 m. The size of the OWSC device and the domain were to replicate the experiments conducted at Queen's University Belfast [28,29], which is for the purpose of validation, as reported in Benites-Munoz et al. [21].

The inlet boundary was set at $x = 0$, where regular waves are continuously generated and propagating towards the positive x-direction, by prescribing the free surface elevation and velocity components according to the Stokes wave theory [30]:

$$\eta = h + \frac{H_w}{2}\cos(kx - \omega t) \tag{1}$$

$$u = \frac{\pi H_w}{T}\frac{\cosh k(z+h)}{\sinh kh}\cos(kx - \omega t) \tag{2}$$

$$w = \frac{\pi H_w}{T}\frac{\sinh k(z+h)}{\sinh kh}\sin(kx - \omega t) \tag{3}$$

where η is the free surface elevation, H_w is the wave height, T is the wave period, h is the mean water depth, k is the wave number and ω is the angular frequency. For the wave properties, H_w and T are given in advance, and the wavelength ($\lambda = 2\pi/k$) was solved by the dispersion relation:

$$k\tanh kh = \kappa, \kappa = \omega^2/g \tag{4}$$

To model an open ocean environment, wave reflections should be avoided at the outlet. This was achieved by applying the active wave absorption for the outlet boundary at the maximal x position [31–34].

For these computational simulations, the total forces and moments come from the fluid and wave loads acting on the body. The fluid forces, $\boldsymbol{F}$, that are considered are the surface forces, $\boldsymbol{F}_s$, as well as the body forces, $\boldsymbol{F}_b$ [35].

$$\boldsymbol{F} = \boldsymbol{F}_s + \boldsymbol{F}_b \tag{5}$$

The surface forces, $\boldsymbol{F}_s$, are calculated from the pressure (hydrodynamic) and viscous forces that come from the normal and shear stresses.

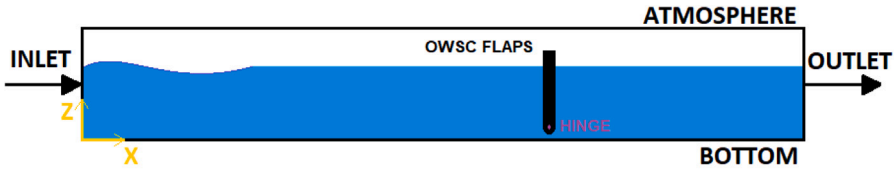

(a) Profile view of the computational setups

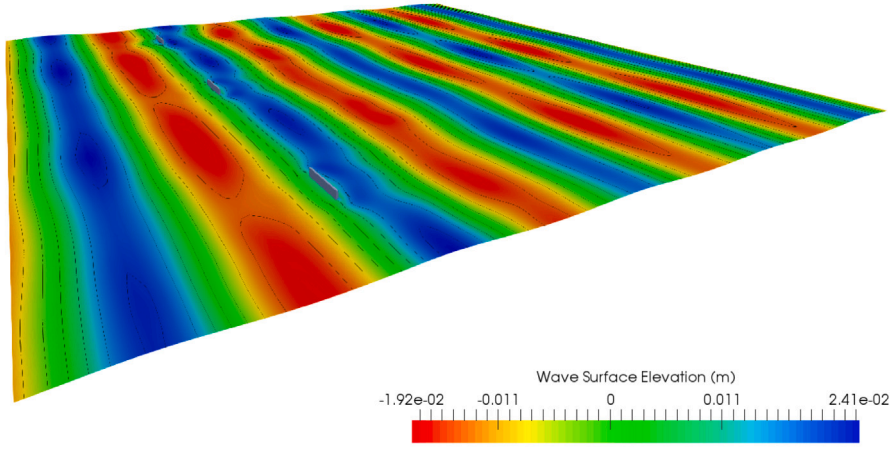

(b) Illustration of a section of the NWT

Fig. 2. Illustration of the computational model of a in-line three-device array.

These forces are calculated at each time-step of the numerical simulation by integrating the pressure and the viscous stress components over the wetted surface of the rigid body, S_B, as follows:

$$\boldsymbol{F}_s = \int_{S_B} (-p\boldsymbol{I} + \boldsymbol{\tau}) \cdot \boldsymbol{n} dS \tag{6}$$

where p is the pressure, $\boldsymbol{I}$ is the unit or identity tensor, $\boldsymbol{\tau}$ is the viscous stress tensor, $\boldsymbol{n}$ is the unit normal vector to the body surface and S_B is the wetted surface. These forces already consider the outer forces related to the interaction of the fluid with the solid body, such as the added mass.

The body forces, $\boldsymbol{F}_b$, include the gravitational force:

$$\boldsymbol{F}_b = m\boldsymbol{g} \tag{7}$$

where m is the mass of the rigid body and $\boldsymbol{g}$ is the acceleration of the gravity vector.

Finally, the total fluid force vector takes the form:

$$\boldsymbol{F} = \int_{S_B} (-p\boldsymbol{I} + \boldsymbol{\tau}) \cdot \boldsymbol{n} dS + m\boldsymbol{g} \tag{8}$$

Similarly, the total moment, $\boldsymbol{M}$, is calculated at each time-step as the sum of all the components acting around the rotation point of the body:

$$\boldsymbol{M} = \boldsymbol{M}_m + \boldsymbol{M}_h \tag{9}$$

where $\boldsymbol{M}_m$ is the mass moment of inertia and $\boldsymbol{M}_h$ is the hydrodynamic moment, which are detailed below.

In Eq. (9), the hydrodynamic moment, $\boldsymbol{M}_h$, is obtained by integrating the pressure and the viscous shear forces over the body's surface at each time step.

$$\boldsymbol{M}_h = \int_{S_B} \boldsymbol{r} \times (-p\boldsymbol{I} + \boldsymbol{\tau}) \cdot \boldsymbol{n} dS \tag{10}$$

where $\boldsymbol{r}$ is the position vector (x, y, z).

The mass moment of inertia, $\boldsymbol{M}_m$, is obtained from the positions of the centre of gravity and the centre of rotation of the device as follows:

$$\boldsymbol{M}_m = (\boldsymbol{r}_c - \boldsymbol{r}_h) \times m\boldsymbol{g} \tag{11}$$

where $\boldsymbol{r}_c$ is the position of the centre of gravity at a time-step and $\boldsymbol{r}_h$ is the hinge position. Thus, the total moment is calculated as:

$$\boldsymbol{M} = \int_{S_B} \boldsymbol{r} \times (-p\boldsymbol{I} + \boldsymbol{\tau}) \cdot \boldsymbol{n} dS + (\boldsymbol{r}_c - \boldsymbol{r}_h) \times m\boldsymbol{g} \tag{12}$$

Now, for a general case, the motion equation for the rigid body is based on the linear and angular momentum equations:

$$\boldsymbol{a} = \frac{\boldsymbol{F}}{m} \tag{13}$$

$$\boldsymbol{\alpha}_b = \frac{\boldsymbol{M}}{\boldsymbol{I}_m} \tag{14}$$

where $\boldsymbol{a}$ and $\boldsymbol{\alpha}_b$, are the linear and angular accelerations, respectively, and $\boldsymbol{I}_m$ is the moment of inertia of the rigid body.

The Newmark time integration scheme is applied to obtain the angular velocity and displacement of the rigid body [36]. The angular velocities and the displacements of the body are obtained from the following equations [37]:

$$\omega_b^{t+\Delta t} = \omega_b^t + \left[(1-\gamma)\alpha_b^t + \gamma\alpha_b^{t+\Delta t}\right] \Delta t \tag{15}$$

$$\theta_b^{t+\Delta t} = \theta_b^t + \omega_b^t \Delta t + \left[\left(\frac{1}{2} - \beta\right)\alpha_b^t + \beta\alpha_b^{t+\Delta t}\right] \Delta t^2 \tag{16}$$

where ω_b is the angular velocity vector of the body, θ_b is the angular displacement vector of the body, γ is the velocity integration coefficient, β is the position integration coefficient, Δt is the time-step, superscript "t" is used for the values obtained on the previous iteration, whilst "$t+\Delta t$" is for the values at the current time being simulated. The recommended value for γ is 0.5 and for β is 0.25 [38]; these are the values used in this work.

The above set of forces and motion equations are for any six-degree motion body. However, it is worth noting that for the case of the OWSC, only one degree of motion is applicable, the pitching motion. Hence, only those equations related to the moment and angular acceleration about the y-axis are relevant for the OWSC.

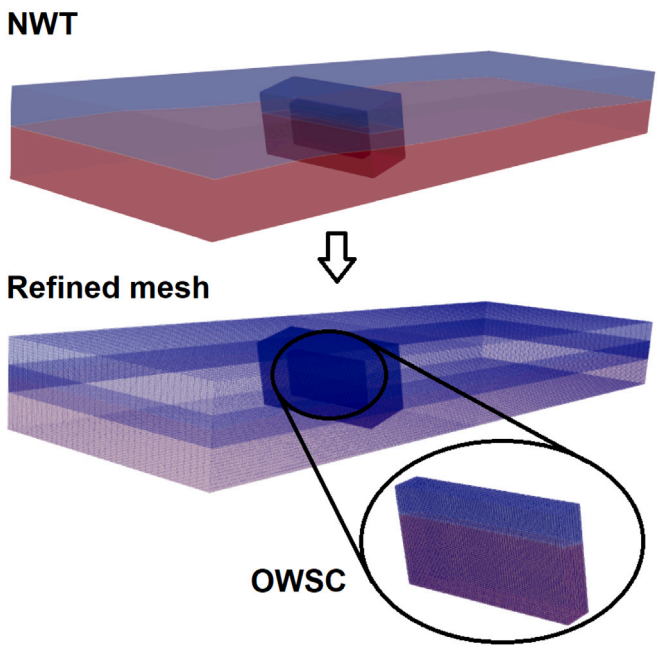

Fig. 3. Mesh view around one OWSC device.

2.2. Solution and discretisation

The fluid field containing the wave-structure interaction of the computational domain is obtained through solving the Reynolds-averaged Navier–Stokes (RANS) equations to obtain fluid velocity and pressure, as expressed in Eqs. (17) and (18).

$$\nabla \cdot \overline{\mathbf{v}} = 0 \tag{17}$$

$$\frac{\partial(\rho\overline{\mathbf{v}})}{\partial t} + \nabla \cdot (\rho\overline{\mathbf{v}}\overline{\mathbf{v}}) = -\nabla\overline{p} + \nabla \cdot (\overline{\tau} - \rho\overline{\mathbf{v}'\mathbf{v}'}) + \rho g \tag{18}$$

where $\overline{\mathbf{v}}$ is the time-average velocity vector (u, v, w), $\mathbf{v}'$ is the fluctuating one, ρ stands for the density, $\overline{p}$ denotes the pressure, $\overline{\tau} = \mu[\nabla\overline{\mathbf{v}} + (\nabla\overline{\mathbf{v}})^T]$ is the viscous term, μ is the dynamic viscosity and g is the gravitational acceleration. As the RANS equations have considered the turbulent fluid, the SST $k-\omega$ model [39,40] was adopted to close the equations.

The free surface between the air and water was modelled by the Volume of Fluid (VOF) method [41]. The VOF method introduces a scalar α, which denotes the fractional volume of a cell occupied by a specific phase. In this case, a value of $\alpha = 1$ corresponds to a cell full of water and a value of $\alpha = 0$ indicates a cell full of air. Thus, the free surface, which is a mix of these two phases, is formed by the cells with $0 < \alpha < 1$. The elevation of the free surface as a function of time is obtained by the advection equation of α, as expressed in Eq. (19). For a cell containing both air and water, its density and viscosity are determined by a linear average of both the fluids, according to Eq. (20) and (21).

$$\frac{\partial\alpha}{\partial t} + \nabla \cdot (\overline{\mathbf{v}}\alpha) = 0 \tag{19}$$

$$\rho = \alpha\rho_{water} + (1-\alpha)\rho_{air} \tag{20}$$

$$\mu = \alpha\mu_{water} + (1-\alpha)\mu_{air} \tag{21}$$

In this study, $\rho_{water} = 1000$ kg/m^3, $\mu_{water} = 1 \times 10^{-3}$ N s/m^2; $\rho_{air} = 1$ kg/m^3, $\mu_{air} = 1.48 \times 10^{-5}$ N s/m^2 and g was set as 9.81 m/s^2.

The Finite Volume Method [42] was applied to obtain the solution of the fluid domain over a certain time duration. The process includes two types of discretisation, in space and time respectively. In space, the computational domain is divided into a set of non-overlapping cells, known as a mesh; in time, the temporal dimension is split into a finite number of timesteps. For a single timestep, the solution of the governing equations can be obtained in each cell (e.g. $\overline{v}$, $\overline{P}$, α), and the whole fluid domain can be integrated by the solution of all cells. Then, the fluid domain over a certain time duration is the composition of the fluid domain at each timestep.

In this study, the computational domain was divided into a hexahedral mesh, as shown in Fig. 3. Local mesh refinements were applied at the free-surface area and the area around the device. An overset mesh was applied around the device which is necessary to enable large rotational movement of the device [43,44]. The mesh of the unrefined region consists of 120 cells per wavelength and 8 cells per wave height, and for the refined region it consists of 240 cells per wavelength and 30 cells per wave height. The selection of mesh densities has been justified through mesh sensitivity studies reported in [21], in order to get accurate solutions with as few cells as possible.

The size of each timestep was determined by a prescribed value, Courant number (C):

$$C = \frac{u\Delta t}{\Delta x} \tag{22}$$

where Δt is the timestep size, $u/\Delta x$ is its normal velocity divided by the distance between the cell centre and the neighbour cell centre. For every timestep, there exists a maximal $u/\Delta x$ value in the domain, and Δt can be calculated by the product of that value and C. This allows an optimal Δt to be selected according to the transient fluid state. The value of C was given as 1 in this study which is a standard practice [45].

Although there has been a lack of experimental tests of multiple OWSC in waves, the present model has been validated against the experimental measurement of a single OWSC device's rotational movement in waves. The systematic verification and validation are presented in a previous publication [21], which is not repeated in the present work to keep it concise. The validation shows the present model can accurately replicate one OWSC' wave-structure interaction with high fidelity, and it is reasonable to deem that the extended wave farm simulations with multiple OWSCs are still validated.

3. Simulation case setups of wave farm

3.1. Array arrangement

In this study, three layout designs were investigated: one in-line (CG1) and two staggered (CG2 and CG3) configurations, as shown in Fig. 4. Each layout considered three independent devices, identified from 0 to 2, and 0 indicates the right-hand side when considering the direction of the incident wave. Additionally, the spacings in the longitudinal and transverse directions were varied and evaluated for different wave periods. It is worth noting that the devices were equally distributed within a single condition, i.e. one X and one Y spacing was considered at a time. In the x-direction, four values were evaluated with a range of distances between 0.00 and 1.56 m. In the y-direction, the range considered was between 0.15 and 3.30 m. In the full-scale model, these values correspond to 0.00–62.40 m for the former and 6.00–132 m for the latter. The distances of X and Y and their nomenclature during the simulations are presented in Table 1; this combination of waves and layouts leads to a total of 116 cases to understand the interaction of arrays within different operational conditions. Each set of spacings combination is identified as $X_k - Y_k$ during the simulations and presentation of the results. The subscript k, from Table 1, provides the identifier ("A" and the numbers 0–8) of the case spacing combination and its nomenclature.

For the in-line layout, CG1, the total number of cases added up to 24, as this arrangement does not consider a displacement in the x-direction, but nine displacements in the y-direction; these combinations were simulated for the wave conditions defined. In addition, for the

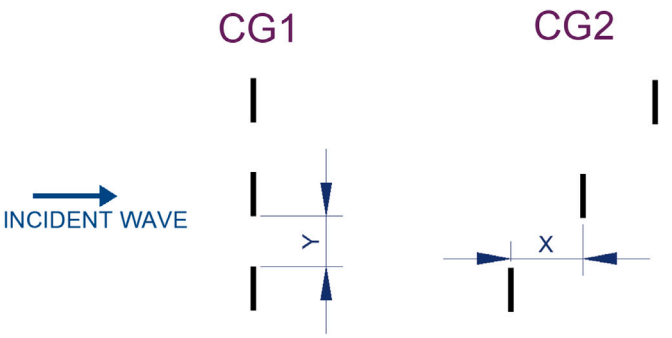

Fig. 4. Plan view: in-line (CG1) and staggered (CG2 and CG3) layouts used during the simulations. The separating distance between the devices 0–2 for the different layouts is varied in the x- and y-direction.

Table 1
Separating distances in the x- and y-direction considered for different wave farm arrangements.

Subscript, k	Combination parameters for arrangements									
	A	0	1	2	3	4	5	6	7	8
X_k (m)	–	0.00	1.08	1.20	1.56	–	–	–	–	–
Y_k (m)	0.15	0.35	0.75	0.95	1.05	1.30	1.50	2.00	3.30	4.30

Table 2
Wave periods and frequencies considered for the study of arrays.

Case, j	1	2	3
Period, T_j (s)	1.344	1.186	1.028
Angular frequency, ω_j (rad/s)	4.68	5.30	6.11
Non-dimensional ω^*	0.87	0.99	1.14

highest period, two further separating distances were considered, to confirm the trend of the power capture performance of the system.

Once the evolution of the performance when varying the separation in the y-direction (lateral distance) was established; the arrangements for the staggered were defined as being sufficient to show the trend of the array. In these cases, each staggered configuration considered 15 arrangements; these combinations were carried out for each wave period. As a result, the total simulations undertaken for the staggered configurations added up to 90 cases.

3.2. Wave conditions

Considering the extensive parameters of the array arrangement, to remain a reasonable size of the simulation matrix, the wave conditions used here consist of one wave height and three periods. The selected periods were chosen based on the higher power delivered by the device within the operational sea state [46]. As a result, for the interaction of neighbouring devices, a range of periods for the regular waves was considered between 1.03 s and 1.34 s, corresponding to full-scale periods of 6.50 s and 8.50 s, respectively, see Table 2. A single height was considered based on the wave height's lower impact on the capture factor in contrast with the period. The wave height was fixed to 0.06 m, which at full scale would correspond to 2.24 m.

3.3. Power take-off

The power extracting component can be modelled as an actuator exerting a mechanical load on the oscillating flap [47], as illustrated Fig. 5). Potentially, the most straightforward approach is to consider only a damper as the energy absorbing load acting on the flap; this is called a passive/resistive control strategy. However, the resistive approach can be complemented with reactive loads controlling the

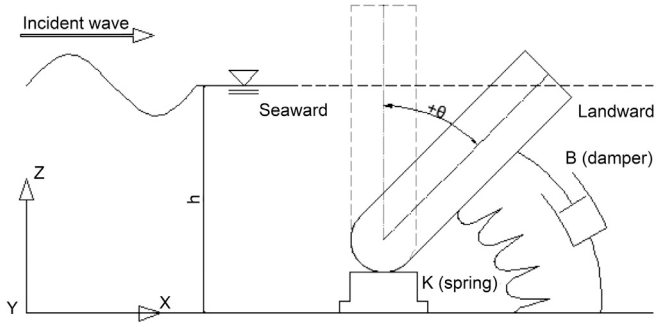

Fig. 5. Schematic profile view drawing showing the motion of an OWSC induced by incident waves, including the spring and damper representations of the PTO.

Table 3
Wave periods considered and the corresponding estimated damping coefficients.

Period (s)		Damping Coeff. (N ms/rad)	
T_1	1.344	B_{d1}	4.13
T_2	1.186	B_{d2}	8.54
T_3	1.028	B_{d3}	8.89

oscillation of the flap to maximise the power extracted [47]. In computational simulations, either passive or reactive control can be realised by adding external moments back to the WEC, represented as a damper or spring–damper system, respectively [48,49]. In the former case, the extracting component is simulated as a force proportional to the angular velocity of the OWSC. Whereas in the latter case, it is an extension of the former, used where an additional force proportional to the angular displacement is integrated into the model [49–51].

In reactive control strategies, the spring and damper coefficients are adjusted according to the real-time wave frequency, thus achieving the maximum power absorption specifically by tuning the stiffness to the natural frequency of the WEC device [49,52]. In this condition, the damping coefficient of the PTO is considered as the radiation damping coefficient of the device. However, as these phenomena of the hydrostatic stiffness and radiation are already considered within the governing equations, an additional method is sought to implement these representative coefficients effectively by maximising the power output of the single device under specific wave conditions.

The PTO for each device considered in the present study was based on a reactive control approach. In the computational model, the PTO is added as a restraint in the motion solution of the OWSC as an external moment as follows:

$$M_{PTO}(t) = B_d\dot{\theta}_i(t) + K_d\theta_i(t) \tag{23}$$

where B_d is the mechanical damping coefficient, K_d is the mechanical spring coefficient, $\dot{\theta}$ is the angular velocity, and θ is the flap rotation around the y-axis. The subscript i refers to the device number within the array, labelled 0, 1 and 2.

Here, B_d is taken as optimal values for an OWSC device in corresponding wave conditions [53], as given in Table 3. The mechanical spring coefficient, K_d, is set up as 9.25 Nm/rad. This coefficient controls the oscillation of the flap through the PTO, and as such, it has been kept constant when optimising the damping coefficient for the single device. Furthermore, these coefficients are used as constants when analysing the array performance.

To calculate the instant net maximum absorbed power by THE PTO for each device considered i, the following equation was used:

$$P_i(\omega) = \frac{1}{2}\omega^2 B_d|\theta_{i,max}|^2 \tag{24}$$

where it is assumed that the power is fully extracted by the PTO (without any mechanical losses), θ_{max} is the maximum amplitude calculated from the numerical model, and ω is the angular frequency. As this

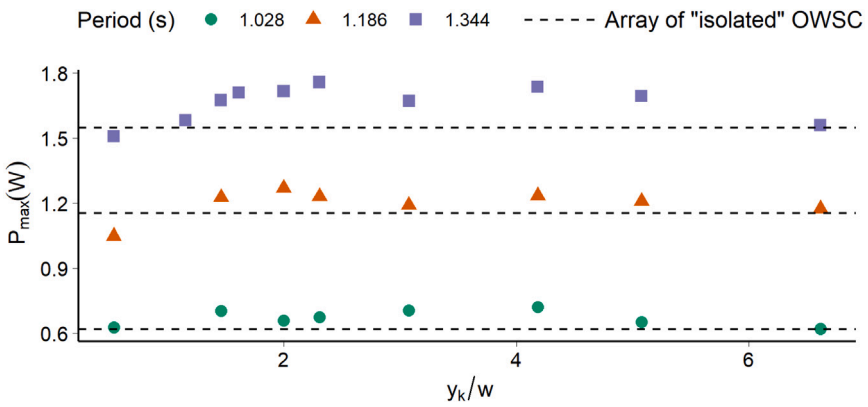

Fig. 6. Maximum power captured by the in-line configuration, CG1, for different periods. Each dashed line is a reference of the power captured by the sum of 3-isolated OWSC devices.

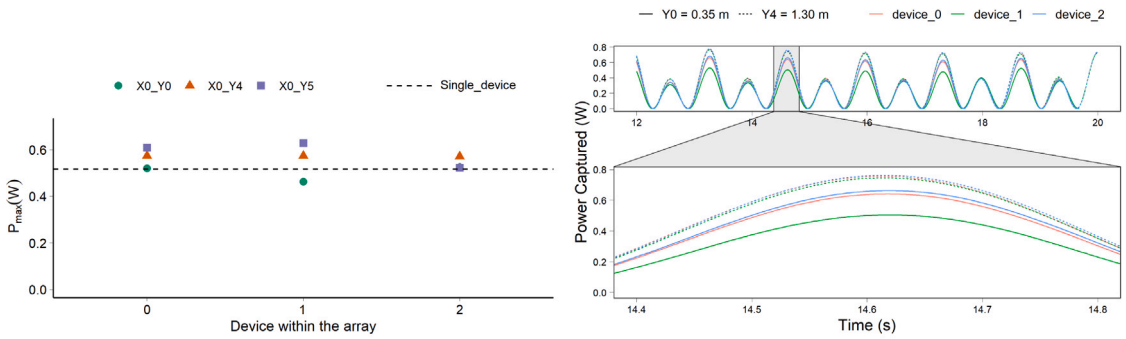

(a) Maximum power absorbed. (b) Power extracted time variation.

Fig. 7. Assessment on the performance of each device of the in-line configuration, CG1, and at different lateral spacings, for T_1.

equation is in the frequency domain for a time-domain simulation, it could lead to slight uncertainties when estimating the time-averaged mean absorbed power due to the different approaches considered.

4. Interactions and power output of neighbouring devices

To analyse the performance of a wave farm this section covers two general approaches, one is the power absorption of the array and the second, although related, is the efficiency in enhancing the operational practices. To do this, each configuration was evaluated against the following criteria. First, the maximum power absorbed was assessed across different wave periods. Second, the wave effects associated to the individual assessment of the devices within the array were analysed. Third, the efficiency of the wave absorption as a unit system was examined using the peak-to-average ratio of power extracted. Finally, the efficiency of the WEC arrays by improving the performance of the systems was addressed using the q factor.

The capture factor q introduced by Budal [54] was used to measure the efficiency of the array. This capture factor relates the net maximum energy production of the array to that of the sum of n devices operating in isolation and should be greater than 1 for the configuration to be successful (constructive interaction). Whereas if q is equal to 1, there is no impact between the devices, and when it is less than 1, the array has a destructive interaction [54,55]. Hence, the constructive interaction of the wave is:

$$q(\omega) = \frac{\tilde{P}_{array}(\omega)}{n\tilde{P}_{isolated}(\omega)} \geq 1 \tag{25}$$

where $\tilde{P}_{array}(\omega)$ is equal to $\sum_{i=0}^{n} P_i(\omega)$, P_i is calculated as described in Eq. (24). $\tilde{P}_{isolated}(\omega)$ is calculated using the results of one WEC simulated in isolation [21].

For any arrangement considered in wave farms, it is expected that if the spacing between the devices is large enough, the modified wave fields will not interact with the adjacent devices, and the cost benefits will decrease. At the beginning of this section, the results per arrangement while varying the spacing are shown to understand the interaction between the WECs as a group and independently. Later, the configurations are compared, narrowing to recommended spacings dependent on the incident wave field. During the analyses carried out, the maximum power was calculated considering the average of the maximum displacements of the device (at the seaward and landward positions), found as $\theta_{i,max}$. The power absorbed by each device was added to estimate the total power captured by the entire array. The average power absorbed was calculated based on each device's mean absolute angular displacement.

4.1. In-line configuration

4.1.1. Power absorbed

Fig. 6 compares the maximum power captured by the in-line arrangement under different periods against the non-dimensional lateral spacing. Whilst the first parameter was calculated using the maximum angular displacement of each device, the latter is presented in terms of the ratio of the lateral separating distance and the device's width, y_k/w. Each set of results for a unique period is accompanied by the reference dashed line representing the maximum power captured by the same number of devices operating in isolation, indicating that the power measured over the line corresponds to a positive interaction. The ones under the dashed line show a destructive interaction. In general, this plot suggests that there is an increment in the variation in the power captured when the period is higher, i.e. when the wavelength increases.

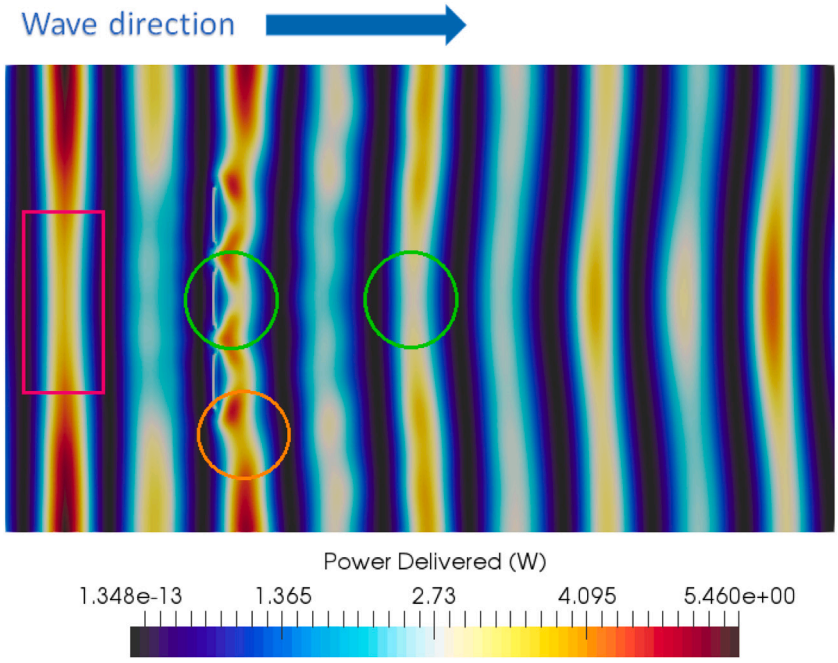

Fig. 8. Plan view of a section of the NWT; the incident wave is from the left side of the plot. Snapshot at 16 s, showing the power delivered by the wave during the performance of the in-line configuration, CG1, when the devices are close and the system is operating destructively (for T_1).

In the same figure, for the highest period, $T_1 = 1.344$ s, it is shown that when the devices are at a non-dimensional lateral separation below or close to 1, the performance of the array is adverse compared to an array considering isolated behaviour. This result suggests that it is not beneficial to consider a wave farm under the layout X_0-Y_0 at this wave period. The behaviour of the in-line layout at T_1 is similarly reproduced for $T_2 = 1.186$ s, whose results are included in the same figure. Whereas for the lowest period, $T_3 = 1.028$ s, the system seems not to reach a destructive interaction under the separating distances considered; yet the improvement and overall magnitude of the power absorbed remain low.

Nonetheless, once the separating distance between the devices is increased, there is a clear constructive interaction occurring in the in-line configuration which applies to all the wave periods, see Fig. 6. Once the lateral spacing is sufficiently large, the devices in the array tend to operate as they would do in isolation without being affected by neighbouring devices. These results provide a general overall response stages of the wave farms until there is no added benefit of deploying the WECs as a compact group.

To examine the contribution per device within the arrays, the power captured by each component is contrasted with that obtained with the single device for T_1. Three layouts are considered, the one where the interaction seems to be destructive, $X_0 - Y_0$, and the ones with the maximum power captured, X_0-Y_4 and X_0-Y_5. These cases correspond to y_k/w equal to 0.54, 2.00 and 2.31, respectively. The results of this contribution per device is presented in Fig. 7(a), where it is shown that the greatest influenced device is the one in the middle (no. 1). In the case of devices 0 and 2, left and right when facing the incident wave, the devices' contribution has lower variation than the other layouts. Additionally, it can be seen that the device in the middle, in layout $X_0 - Y_0$, has a destructive interaction compared to the single WEC (represented with the dashed line), which may affect the overall behaviour of the array.

The progress of the power captured by the arrays when y_k/w is equal to 0.5 and 2 are shown in Fig. 7(b), for T_1. The resulting curve for each device in the array is shown for an interval between 12 and 20 s; nonetheless, at a selected time around the peak values (presented at 14.6 s) the results are highlighted for the purpose of visualisation. Generally, it can be seen that the return power captured (at the seaward angle position) is lower than the one towards the land. This behaviour in the resulting power delivered by the devices is distinctive when applying reactive control strategies to represent the PTO. In addition, it can be seen that when $y_k/w = 0.5$ $(X_0 - Y_0)$ the power absorbed by the middle device is considerably lower than that obtained by the devices located at the extremes. Whereas in contrast, in the case of $y_k/w = 2.0$ $(X_0 - Y_4)$ each unit remains rather constant compared to the neighbouring ones.

To identify what is causing this decline in the power absorbed by the device at the centre; it is important to examine the direct factor, which is the reduction in the angular displacement of the device. Fig. 8 shows layout X_0-Y_0 when the time of simulation is 16 s, and the WECs have an angular displacement of 5.35°, 4.74° and 5.49°, for devices 0, 1 and 2, respectively. The power delivered by the wave was estimated using Equation ??, using the surface elevation measurements. In this setting, the flow between the OWSCs is trapped, and transmitted waves in the back of the devices arise due to the positive angular motion of the array; which are comparatively lower in the device at the centre. For this purpose, the green circles in the figure highlight the reduction in the power delivered behind the middle device. In this case, the wave effects presented between the components seem to negatively impact the wave power delivered at this unit (device no. 1). In addition, it can be seen that the power delivered by the source decreases considerably downstream, once it has been absorbed by the array. The influence on the middle WEC can be confirmed afterwards in Fig. 10(a), where the q factor of the wave farm under this layout and wave conditions is below 1, i.e. the overall performance of the array is destructive.

In addition, in Fig. 8, it can be seen that the radiated waves upstream have a negative interaction with the incident wave field, bringing down the power available in this area (see pink rectangle). Another interesting effect of the WEC's presence are the diffracted waves, which can be seen to the sides of each WEC. In this case, there is a localised reduction in the wave energy, see orange circle. Whilst the effects related to the radiated and transmitted waves seem not to influence the neighbouring devices in this particular layout, the ones related to the diffracted waves, seem to have an immediate influence towards the devices at the sides. Thus, the device at the centre is the most benefited or negatively affected during the process.

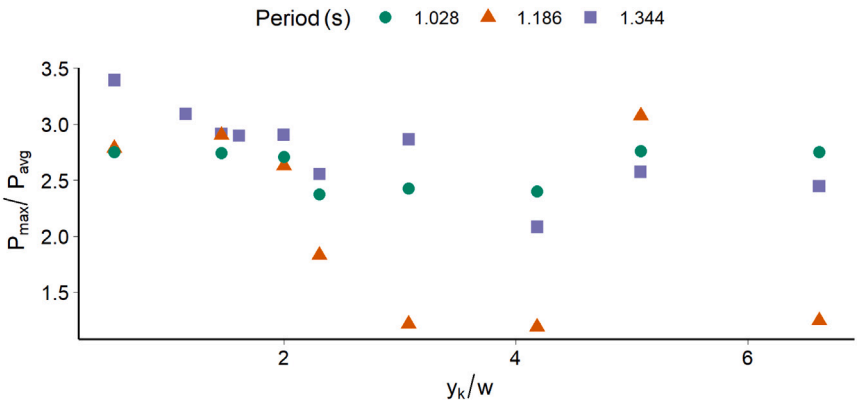

Fig. 9. Peak-to-average ratio of the power captured by the in-line configuration, CG1, for different periods.

Fig. 9 provides insight regarding the ratio between the maximum and average power captured by the in-line arrangement to further examine the absorption efficiency of the system. These results are presented for all the periods assessed. For an efficient system, the desired value of this ratio should remain low. For the largest distances between the devices ($y_k/w > 2.3$) the results show a higher variation depending on the period. In contrast, it can be seen that for shorter separating distances in the y-direction, the behaviour of the array is more consistent against different periods. In the cases where P_{max}/P_{avg} approaches 1 (for T_2), it seems to suggest that in these conditions, the power delivered is more stable and efficient.

4.1.2. Absorption enhancement for the in-line layout

To select a system where the overall performance of the array is enhanced, the q factor is investigated. The q factor for different lateral spacings is shown in Fig. 10(a), where it can be seen that there is a drop in the power capture in $y_k/w = 3.1$ after the highest peak ($y_k/w = 2.3$). In this dip (at $X_0 - Y_6$), the rotational displacement of the centred device is not enhanced by its neighbours, decreasing the overall performance of the array. However, the variation in this drop compared to the next increasing value is minimum when considering this as a positive/negative effect in the interaction. Additionally, these results do not lead to an exact ideal distance between the neighbouring devices, but a range of $1.2 < y_k/w < 5.0$ where the interaction is beneficial up to 15%, see the trend shown with the dashed line for these results in Fig. 10(a).

A behaviour similar to that of T_1 is reproduced for the lower periods (for $T_2 = 1.186$ s and $T_3 = 1.028$ s), which are presented in Fig. 10(b). In both cases, the dip in the performance occurs at different lateral spacings; whilst for T_2 this happens close to $y_k/w = 3.1$, for T_3 is at a shorter separation ($y_k/w = 2.0$).

4.2. Staggered configurations

4.2.1. Power capture

The staggered configurations, CG2 and CG3, consider a displacement in the longitudinal direction (along the x-axis) as well as the lateral distance. Fig. 11 compares the maximum power absorbed by the staggered arrays, CG2 and CG3, at a longitudinal separation between the WECs, $X_3 = 1.56$ m, for different periods. The values of the separating distance in the y-direction have been chosen in accordance with the trend seen before in the in-line configuration, i.e. defining a region for constructive interaction after which the values of the power absorbed decline. In addition, each set of results is accompanied by a dashed line showing the absorption power that would be achieved by a set of isolated devices under a specific wave period.

In this particular longitudinal separating distance, X_3, it is shown that for longer waves, the performance of the staggered systems remains positive (over the dashed line). In contrast, for the middle and lower periods, it seems that there is not sufficient increment in the power absorbed by the systems. Additionally, it can be seen that for the lower periods, there is a negative behaviour as a group, as the power has been reduced. What is also interesting in these plots is that for the asymmetric and symmetric staggered systems, CG2 and CG3, the trend of the performance is similar in terms of the magnitude and overall response, see Fig. 11.

The contribution of each device in the power capture under different layouts, in terms of staggered configuration and lateral separating distance, is presented in Fig. 12 for a particular longitudinal distance ($X_3 = 1.56$ m). For this purpose, the ratio of the maximum power absorbed by each device within the farm against that of the isolated device is shown; if the ratio is equal or greater than one, it is expected that its individual response is constructive. At the top of the figure, the results for the asymmetrical layout CG2 are included; this arrangement considers that the three devices are at different positions along the x-axis. At the bottom is the symmetrical staggered layout, CG3, where two of the devices perform along the same x-axis, see Fig. 4. It is worth noting, that the slight fluctuation per device in the y-axis shown in Fig. 12 is for visualisation aid and does not have any relevant meaning.

When assessing the unit's behaviour, in most scenarios, besides of the CG2 case for T_1, it is found that the middle device, identified as "device 1", has a destructive performance (<1) at short separating distances, see Fig. 12. Furthermore, in CG2, this is extended to the third device (the one located closer to the shore); which at the lowest period it does not even achieve "isolation-type" performance and remains having a destructive operation.

In contrast, the performance of the device at the front, "device 0", seems to be highly constructive at most scenarios. This result suggests that the undisturbed wave field and the reflection/radiation wave effects of the immediate device play an important role. Likewise, it suggests that during this interaction between the devices, the devices downstream remain at a disadvantage.

An example of these implications is the CG2 case for T_3 with a layout $X_3 - Y_7$, where the devices no. 1 and no. 2 operate destructively as units, whilst device no. 0 has a somewhat "isolation-type" performance (where the ratio is close to 1), see Fig. 12. To investigate this further, the distribution of the power delivered by the wave, in Watts, is shown in Fig. 13. In this setting, the snapshot of a section of the NWT is at 19 s, when the devices have low angular displacements: 1.33°, 0.40° and −0.11°, for devices 0, 1 and 2, respectively. It can be seen that before the first WEC interacts with the incident wave field, the latter remains largely undisturbed across the width of the NWT. However, once the energy of the wave has been extracted by the first device, the conditions downstream are largely influenced. This results in the device further in the system facing a lower-amplitude wave than the original one, likely reducing its power extracted. In addition, at this instant, the power delivered is increased when facing the devices, particularly for device no. 0. Possibly, this is due to radiating waves upstream.

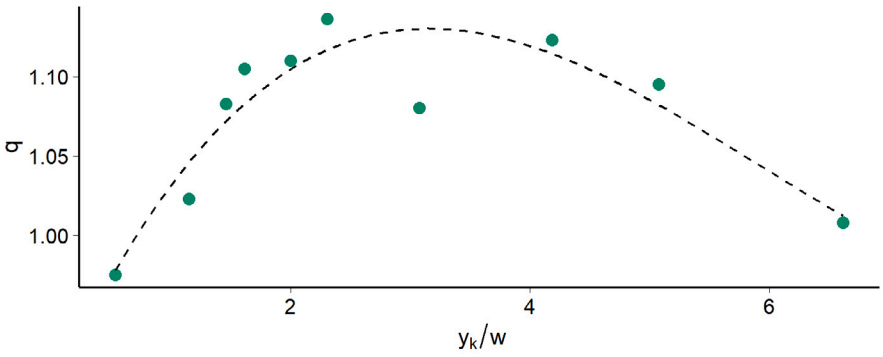

(a) T_1

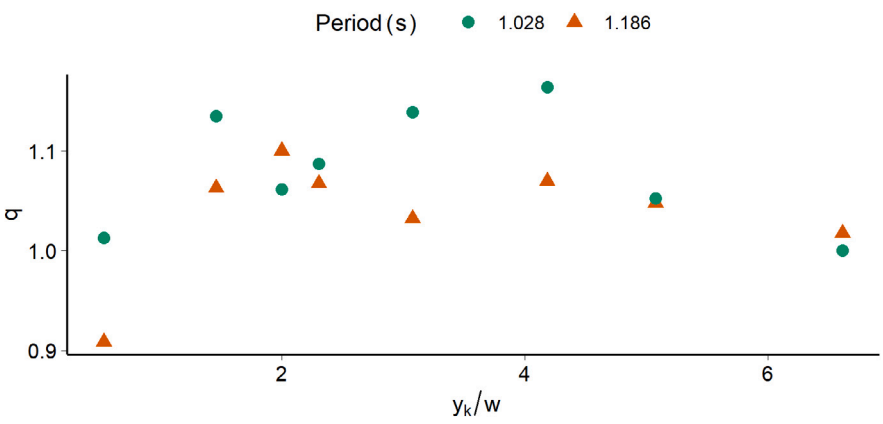

(b) T_2 and T_3

Fig. 10. q factor estimated for the in-line layout, CG1, against the non-dimensional separating distance. The dashed line in (a) show the trend of the performance.

To confirm that there is no influence of the walls, a wider tank has been analysed and presented in Fig. 14. The width selected is then confirmed to be 14.25 m (3 m more than the previous). Similar to Fig. 13, the same hydrodynamic response of the array is seen based on the power delivered by each device. Furthermore, it can be seen on the left side of device no. 0, the one closer facing the incident wave first, that there is no potential reflection of the walls, only the radiated and diffracted waves resulting from the device and its interaction with the incident wave.

To assess the efficiency of the system in terms of absorbing the power of the device, the peak-to-average power ratio of layouts CG2 and CG3 is assessed, see Fig. 15. An important consideration is that for this study, the maximum power absorbed by the device is estimated using the maximum displacement of the WEC; whereas the average power is found using the mean absolute angular displacement. It is expected that the most efficient system in absorbing the wave energy is when the ratio P_{max}/P_{avg} tends to 1. In Figs. 15(a) and 15(b), the highest ratio obtained for T_1 is close to 3, for both staggered configurations, whereas for T_2, it is 2.5. Compared to the results obtained for the in-line configuration, previously presented in Fig. 9, the results of the staggered configurations show similar trends, where it is shown that for the middle wave period the system is more efficient (lower ratio).

4.2.2. Absorption enhancement for the staggered layouts

For CG2 and CG3, at the distance corresponding to X_3, the results for the q factor for different wave conditions are shown in Figs. 16(a) and 16(b), respectively. In this plot, the results of power efficiency for each staggered array will depend on the incident wavelength and the lateral spacing between the devices. It can be seen that when the devices are too close, the interaction of the array is negative (<1). In contrast, for greater distances, the power of the array increases, bringing them to interact positively. Furthermore, it can also be seen that the array operates similarly for the different wave frequencies and configurations at the furthest distance shown. Likewise, a similar general conclusion, but differing in the magnitude of the enhanced power captured and the lateral spacings, happens for the greater spacings in the x-direction.

To further investigate the interaction of staggered systems, the q factor results in terms of the non-dimensional spacings in the x- and the y-direction for different arrangements and wave conditions are shown as surface plots. These plots, Fig. 17 (for CG2) and Fig. 18 (for CG3), gather the information of different spacings in both directions and quantify the power enhanced by each layout and wave condition.

Focusing on Fig. 17(a), which presents the results of CG2 operating under the highest period, the largest q factor is when the non-dimensional lateral distance, y_k/w, is close to 2, and when the devices are further apart in the x-direction. The latter is represented as the non-dimensional parameter x_k/λ, where λ is the wavelength. In addition, when the devices are too close in both directions, the enhancement in the power absorption remains low. This behaviour is similarly reproduced for the lower periods, Figs. 17(b) and 17(c), in terms of the lateral spacing distance, but opposite in terms of the longitudinal distance. For T_2 and T_3, the power capture is boosted for closer non-dimensional separating distance, x_k/λ. This is particularly reproduced to a some extent in CG3, see Fig. 18, where the highest q factor converges to a single non-dimensional lateral distance, $2 < y_k/w < 3$, but differs in the x-direction depending on the wave period.

Thus, from these surface plots it can be seen that regardless of the arrangement (CG2 or CG3), the spacings seem to be of greater influence on the performance of the array for each wave period than the in-line configuration (CG1). For the lower periods, the maximum positive

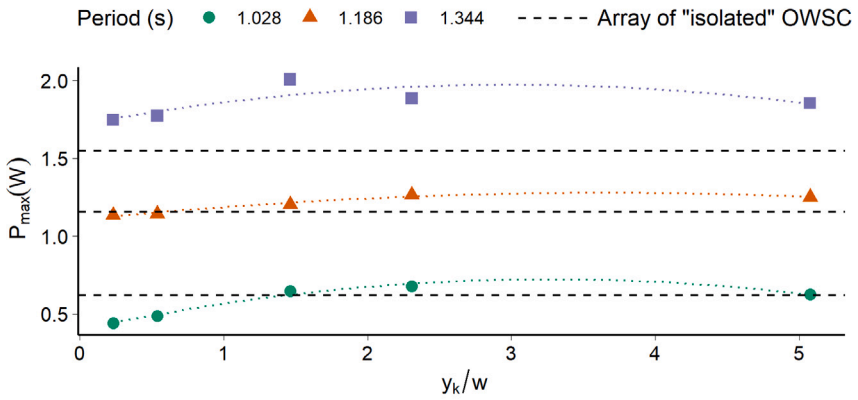

(a) Layout CG2.

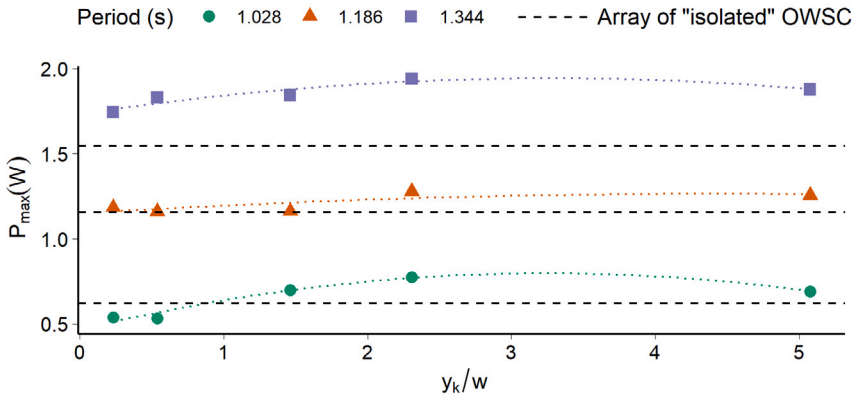

(b) Layout CG3.

Fig. 11. Maximum power captured by the staggered configurations. Each dashed line is a reference of the power captured by the sum of 3-isolated OWSC devices. The coloured dotted lines show the trend of each set of results. The longitudinal separating distance is $X_3 = 1.56$ m.

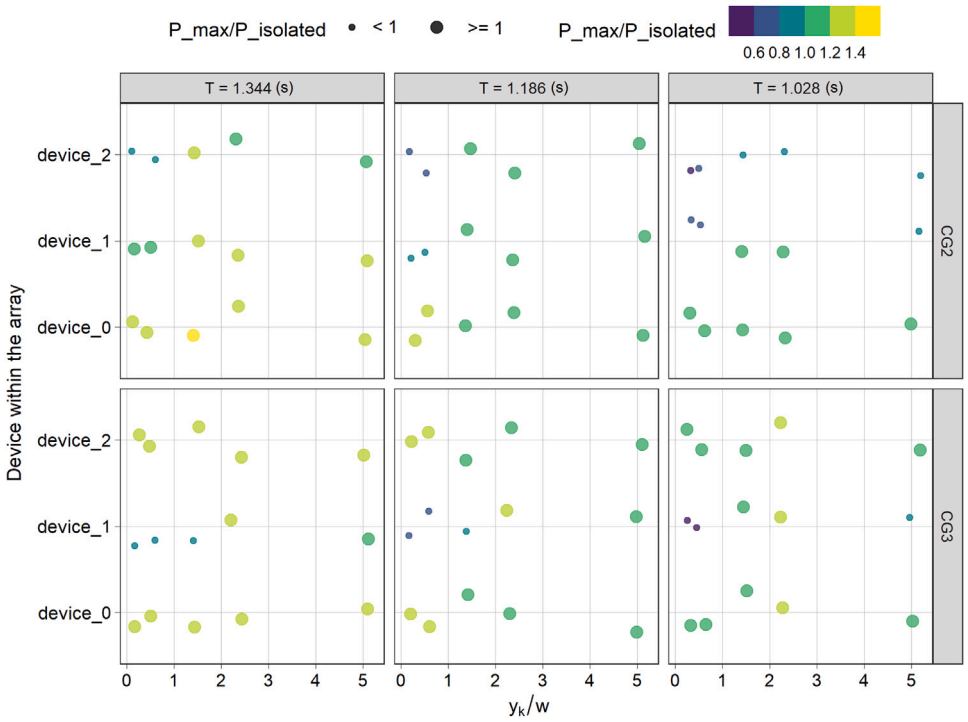

Fig. 12. Ratio of the maximum power captured by each independent device within the farm array against the isolated device. This ratio is given for each staggered configuration and period analysed, for a longitudinal distance of $X_3 = 1.56$ m.

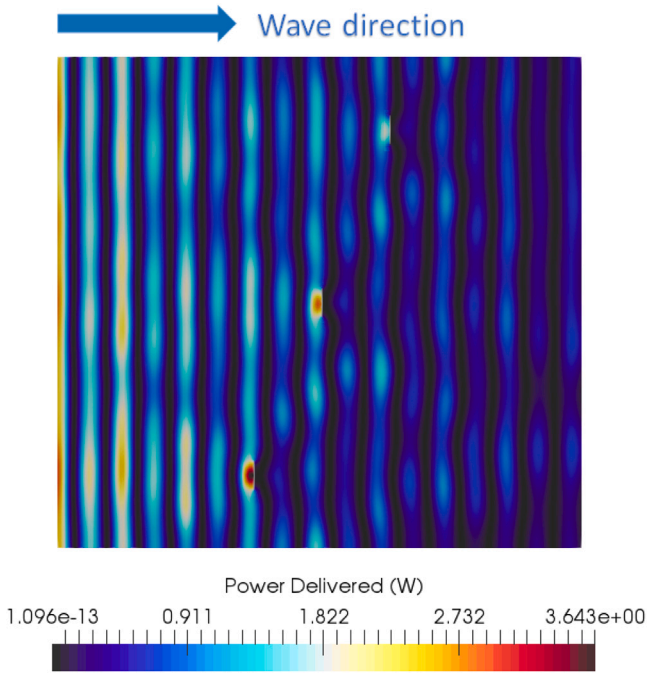

Fig. 13. Plan view of a section of the NWT; the incident wave is from the left side of the plot. Snapshot at 19 s, showing the power delivered by the wave during the performance of the asymmetrical staggered layout, CG2, when the devices are far and the system is operating destructively (for T_3).

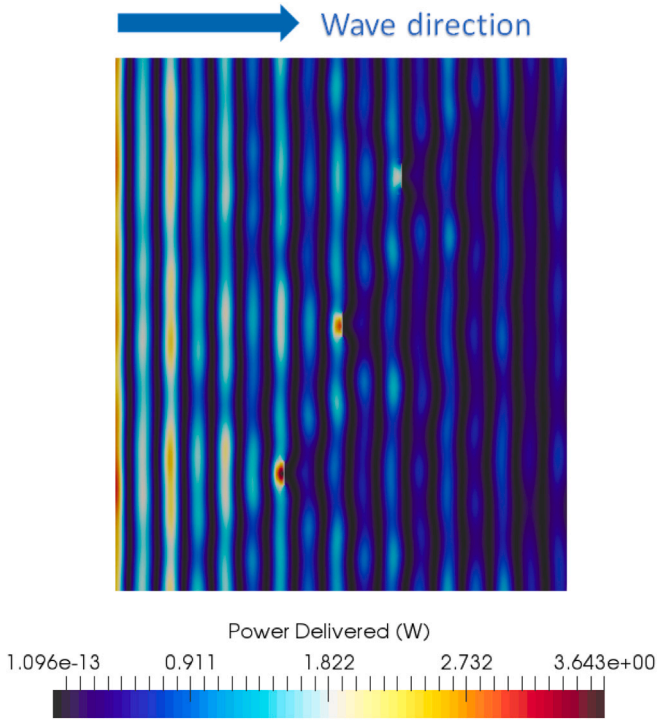

Fig. 14. Plan view of a section of a wider NWT; the incident wave is from the left side of the plot. Snapshot at 19 s, showing the power delivered by the wave during the performance of the asymmetrical staggered layout, CG2, when the devices are far and the system is operating destructively (for T_3).

interaction is when the devices are closer in terms of the longitudinal spacing in both configurations (CG2 or CG3). Whereas for the higher period, the same happens when they are further away.

From analysing the results obtained, it is evident that a particular configuration and distance will not satisfy the maximum power captured for all sea conditions. However, a set of combination parameters can be suggested for the most common sea state that the array will operate in.

4.3. Assessment of layouts

An outcome from the analysis of all the layouts is that when the devices are close in the y-direction, the wave farms perform destructively. Fig. 19 presents the q factor against the non-dimensional longitudinal distance for a close separating distance in the y-direction, $Y_0 = 0.35$ m ($y_k/w = 0.54$), for all the layouts and wave periods. In addition, the destructive region (when $q < 1$) is highlighted. Besides that the in-line arrangement, CG1, in this scenario, the system operates negatively for shorter wavelengths (corresponding to the lower periods). In contrast, the one with the largest wavelength tends to operate positively regardless of the staggered arrangement used.

From the surface plots shown in Figs. 17 and 18, it was found that the greatest constructive interaction is when y_k/w is in the range of $2 < y_k/w < 3$ for all the staggered arrangements and periods. In Fig. 20, the q factor is shown at the lateral spacing Y_5, equal to 1.5 m ($y_k/w = 2.3$), and for all the configurations and longitudinal spacing in terms of the distance over the wavelength, λ. At this condition, it can be seen that the configuration giving the least constructive interaction is CG1, the in-line configuration. Additionally, it can be noticed that for both staggered configurations, when x_k/λ is in the range of 0.55–0.70 (see Box 1), the q factor remains with minor variations regardless of the wave frequency. Furthermore, although the q values of T_3 in Box 2 are greater than 1, these are not relevant since the power captured at this condition is significantly lower compared to the higher periods. As a reference, see Fig. 11 where the quantification of the power captured by the staggered arrangements at this condition (T_3) is shown.

For this particular distance, $y_k/w = 2.3$, it is concluded that in terms of the spacing in the x-direction, the ideal range of x_k/λ is between 0.50–0.75, which for T_1 would be 1.07–1.61 m (42.80–64.40 m at full-scale). Likewise, for T_2, this range would correspond to 0.91–1.36 m for the model (36.4–54.4 m at full-scale). Despite, having a less enhanced result, for the same condition, T_3 would be at around $x_k = 1.10$ m (44 m at full-scale).

Now, focusing on the lateral spacing, y_k/w, the range of separation is greater before the constructive interaction decreases, as seen previously in Fig. 16 for X_3. In this case, the suggested range of y_k/w is between 1.5–5.1, which corresponds to the y-spacing in the model to 0.95–3.30 m (38–132 m at full-scale). After this range, it is expected that the devices within the wave farm would have a similar hydrodynamic response as single units. Based on the spacing ranges in the x- and y-direction, the power captured can be increased from 10% to 25% when operating under these conditions; nonetheless, this is further analysed in the next section.

In Fig. 21, the wave surface elevations of two configurations (CG2 and CG3) are shown, corresponding to Y_2 or $y_k/w = 1.50$ at 17 s of the simulation where the enhancement of the power captured as an array has been increased by 28%, for CG2, and 19%, for CG3. The NWT is shortened to the half of the length for visualisation purposes.

In the case of the asymmetrical staggered layout, CG2, which has a higher capture ratio, it can be seen that the absolute amplitude of the wave has been increased in comparison with the case of CG3. An example of this is the WSE measured at the location of device no. 1, see regions highlighted with pink circles. Considering the snapshot is at the exact time and under the same operational characteristics, the region in front of the middle device at CG2 suggest it is interacting with a higher wave amplitude. Nonetheless, the factor that seems to affect the

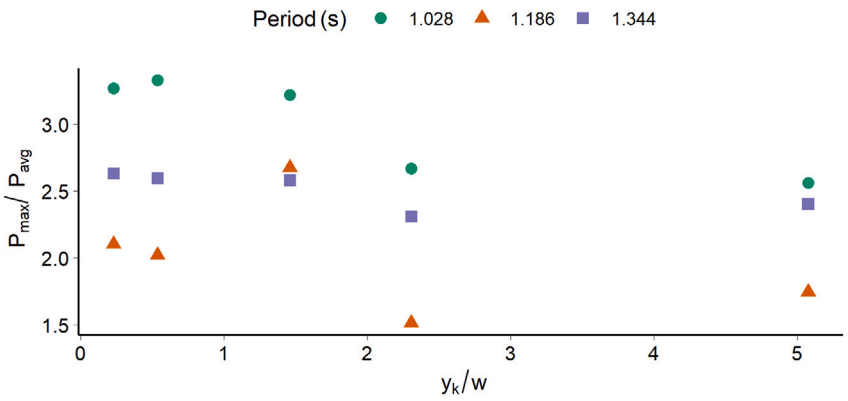

(a) Layout CG2

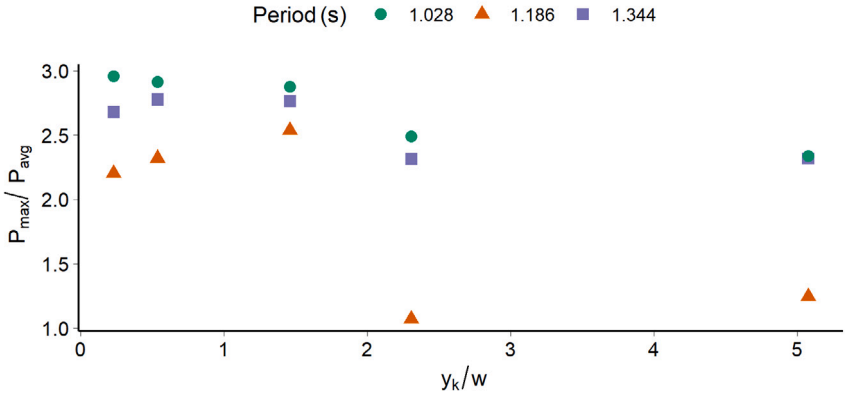

(b) Layout CG3

Fig. 15. Peak-to-average power ratio of the staggered configurations, CG2 and CG3, at a distance X_3 = 1.56 m for varying non-dimensional lateral spacing. These results are shown for different periods.

most is that encountered in device no. 2 (Fig. 21(a)), see black circle, considering there is a higher wave amplitude causing a higher motion in comparison to that same device in CG3 (Fig. 21(b)). As a result, this implies a constructive interaction between the incident and radiated wave (upstream) happening for the device closer to the shore.

5. Discussion of constructive array arrangements

The previous sections investigated the performance behaviour of wave farms arranged in diverse settings. Among the key findings derived from this analysis are the following:

- The in-line configuration showed the smallest hydrodynamic-based performance enhancement when operating with different wave periods. Nonetheless, in terms of the separation of devices, it has a broad range of $1.0 < y_k/w < 5.1$ to increase the power extracted up to 13.6%. In terms of the full-scale prototype, this would imply an interval in the y-direction of $26.0 < y < 133.0$ m where the diffracted waves between the units enlarge the motion of the neighbouring devices.
- In contrast, the staggered configurations generally show better performance than the in-line configuration. However, these systems also show destructive behaviour when operating too close in lateral and longitudinal directions, particularly for the lower periods (shorter wavelengths). Overall, the recommendations for the staggered configurations would consider a range in the y-direction of $1.5 < y_k/w < 5.1$ and in the x-direction of $0.50 < x_k/\lambda < 1.10$. In the latter, it is the lower period that reaches "isolation behaviour" for CG2 at the largest distance in the x-direction; the remaining arrangements stay productive. In terms of the dimensional distances, the considerations for each staggered arrangement are summarised using Fig. 22.

Fig. 22 shows the distance at full-scale in the x- and y-axis and the values of the constructive interaction (when $q > 1$). Likewise, the blank spaces represent the conditions where the arrangement has a destructive performance. A particularly interesting result from the staggered arrangement CG3 is that all the spacings and wave conditions bring a productive operating system ($q > 1$) even if this improvement is minimal (as seen in the shortest separating distances for the lowest period). It can be seen that the efficiency of the array when compared to one considering "isolation-type" devices, is improved for both staggered layouts. In the case of the asymmetrical layout, CG2, the highest q value is obtained for a longer wavelength and for separating distances of $X = 62$ m and $Y = 38$ m. This is similarly reproduced for the symmetrical layout, CG3, but achieving a slightly lower q value. In contrast, this is maintained for this latter layout with the lowest wave period. In addition, it can be seen that for the wave period of 7.50 s, both staggered configuration show similar magnitude in the enhancement for the separating distances $Y > 38$ m.

Since the results shown in Fig. 22 are somewhat similar, an additional analysis is carried out by comparing the two sets of q factor results for each configuration under the same separating distances conditions using a Welch t-test. From the results obtained, it is found that the difference between the data sets of CG2 (mean = 1.073; SD = 0.0147) and CG3 (mean = 1.091; SD = 0.0103) is not significant ($t(85) = -0.765$; $p < 0.447$). The high value of p implies that there is no statistical evidence suggesting sufficient variability in the values contrasted.

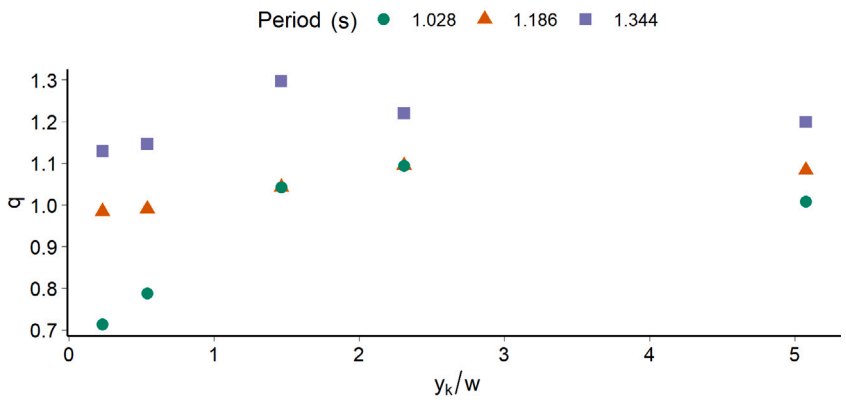

(a) Layout CG2.

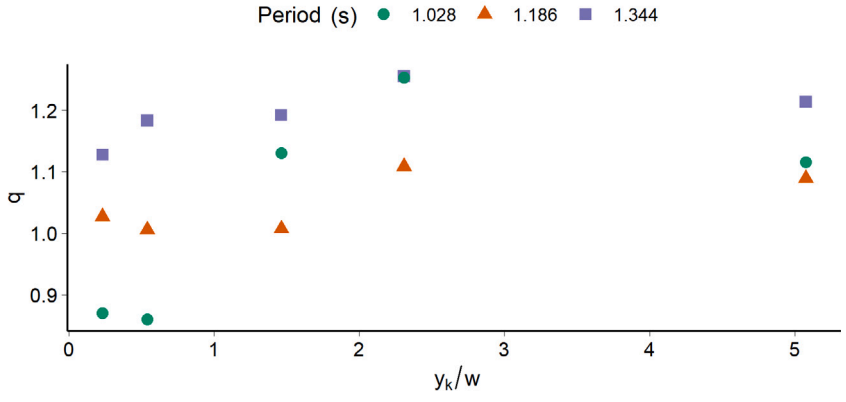

(b) Layout CG3.

Fig. 16. q factor estimated for staggered layouts at a distance in the x-direction of 1.56 m between the devices against the varying non-dimensional lateral spacing.

The present study coincides with the semi-analytical work developed in Noad and Porter, and, Behzad and Sanaei [11,56] where the staggered arrangements suggest leading to more productive wave farms. However, it contradicts the original wave farm arrangement used for the Oyster 2 (composed of three in-line devices) and the most robust interaction in such configuration mentioned in Sarkar et al. [14]. Nonetheless, it is worth noting that there is a high impact on the lateral distance in the power captured by the system. Still, to exploit it, it is suggested to combine it with a displacement in the longitudinal direction.

When contrasting the spacings between the WECs resulting from previous studies on OWSC-array configurations, such as the semi-analytical works presented in [11,15,56], the results are in the same order of magnitude but differ in the intervals recommended. For Sarkar et al. [15], the range for a continuous positive interaction is 0–50 m in the x-direction and 75–100 m in the y-direction. Likewise, Noad and Porter [11] identified a specific optimal spacing of 51.7 m in the x-direction and 40.9 m in the y-direction for a representation of a asymmetrical staggered layout. Moreover, Noad and Porter [11] found the distances of 50.4 m (x-direction) and 37.6 m (y-direction) for a symmetrical staggered layout. Finally, Behzad and Sanaei [56] concluded that for a staggered layout having the highest power extracted, the units should have a spacing of 25 m (x-direction) and 15 m (y-direction). The study carried out in this paper results in a broader interval in the lateral spacings (being this 38–132 m) and discards closer proximity in the longitudinal direction, below 48 m.

Given that there is no unique solution of the staggered configuration bringing the highest performance to capture the wave energy, it is sought to recommend a system based on the response in the constructive behaviour region across all periods. For CG2, the mean q factor is 1.13 and the constructive range is 1.01–1.30. Whilst for CG3, the mean q factor is 1.12 and the constructive range is 1.01–1.26. The asymmetrical staggered configuration, CG2, show the highest enhancement overall by a slight margin and the power is enhanced by 4% more than the symmetrical one. Thus, Fig. 23 provides with the arrangement parameters of the most productive solution, CG2, along with the separating distances achieving the greatest power absorbed. The separating distances are recommended for an interval period of 6.50 s $< T <$ 8.50 s.

6. Conclusions

This paper provides significant insights into the interaction of wave energy converters when operating as a wave farm. A total of 116 cases covering three different layouts and wave periods with various spacing combinations between the devices within the wave farms were selected to assess the enhancement when introducing neighbouring devices to a single WEC system.

One key outcome of this study is that staggered arrangements perform better than in-line arrangements. Furthermore, using staggered configurations, the efficiency of power capture of wave farms can be increased up to 30% when the devices operate constructively, and the distance between the devices is dependent on the incident wave characteristics.

It is found that the wave effects associated to the interaction of the incident wave field with the devices are major contributors in the

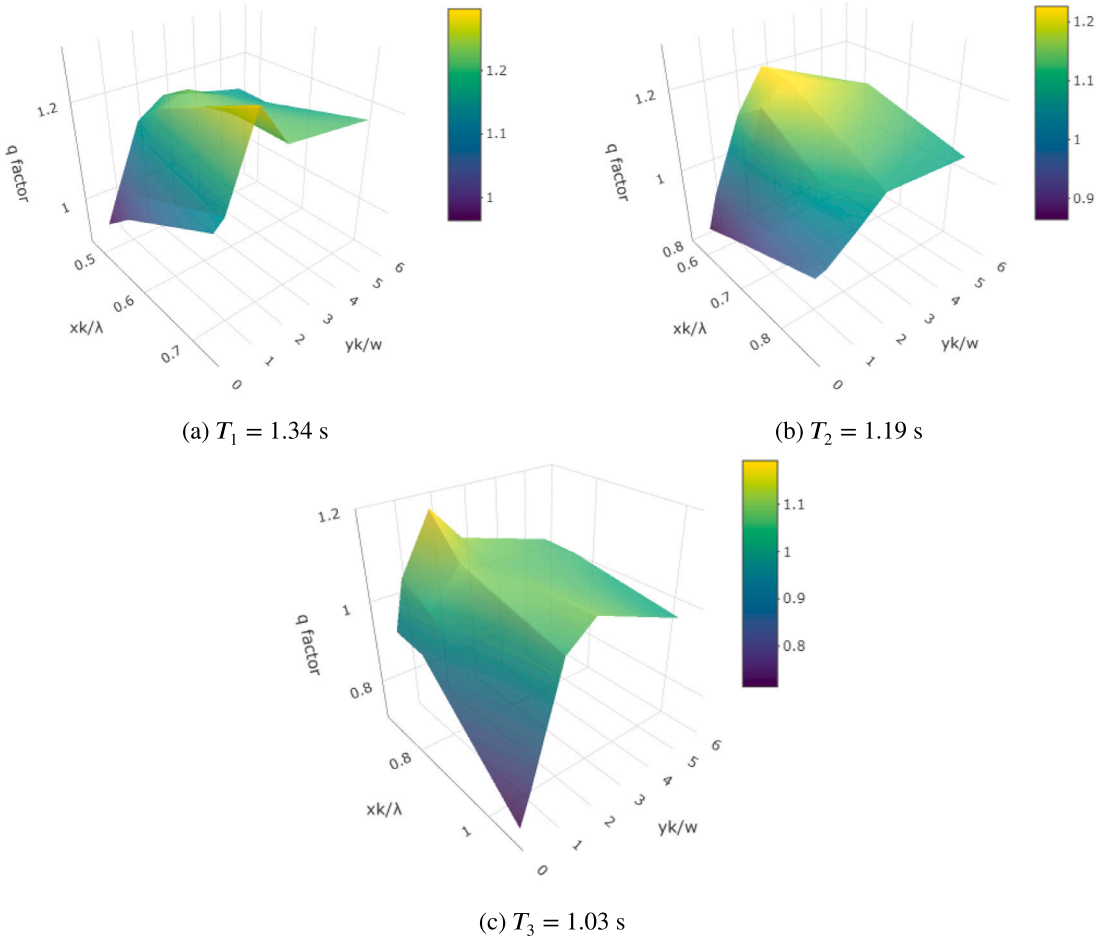

(a) $T_1 = 1.34$ s

(b) $T_2 = 1.19$ s

(c) $T_3 = 1.03$ s

Fig. 17. Surface plots showing the variation of the q factor estimated for layout CG2 operating under different periods. The interaction factor is shown in terms of the non-dimensional distances x_k/λ and y_k/w.

constructive operation of the array. In the case of staggered layouts, the wave energy has been partially extracted by the front device and transmitted to the devices downstream. Depending on the separating distance, this wave with modified energies should be sufficient to allow the devices downstream to operate constructively as a single unit. These results led to a set of intervals in the x- and the y-direction, where the behaviour of staggered layouts is constructive. Nonetheless, the symmetrical and asymmetrical staggered configurations tend to behave similarly in the operational conditions considered; hence, a unique solution could be based on selection parameters, such as a compact arrangement or operational wave conditions desired.

Finally, it is found that when locating the units too close within the wave farm too close, $Y < 38$ m and $X < 48$ m, the efficiency of the system decreases and the interaction in absorbing the waves' energy becomes destructive. Furthermore, it is identified that for the three-OWSC array, the most affected and decisive device in both constructive and detrimental outcomes is the one operating in the middle. For the asymmetrical staggered layout, CG3, this is extended to the device located closer to the shore.

This study considers regular waves as a first step to understanding the interaction of multiple devices operating simultaneously, using high-fidelity tools, such as those provided by a full-dynamic computational model. However, in order to contribute to the concept and early design of OWSC wave farms, a study considering irregular waves is recommended for future work. It is worth noting, that these considerations will impact the model's computational and simulation time capabilities.

CRediT authorship contribution statement

Daniela Benites-Munoz: Conceptualization, Methodology, Software, Validation, Formal analysis, Investigation, Resources, Data curation, Writing – original draft, Writing – review & editing, Visualization. **Luofeng Huang:** Conceptualization, Methodology, Software, Investigation, Resources, Writing – original draft, Writing – review & editing, Project administration. **Giles Thomas:** Conceptualization, Methodology, Investigation, Resources, Writing – review & editing, Supervision, Project administration.

Declaration of competing interest

The authors declare that they have no known competing financial interests or personal relationships that could have appeared to influence the work reported in this paper.

Data availability

All data underlying the results are available as part of the article and no additional source data are required.

Acknowledgements

D.B.M. acknowledges her PhD scholarship provided by the Ecuadorian National Secretary of Higher Education, Science, Technology and Innovation (SENESCYT) and the Escuela Superior Politécnica del Litoral (ESPOL). L.H. acknowledges grants received from Innovate UK (No. 10048187, 10079774, 10081314) and the Royal Society (IEC\NSFC\223253, RG\R2\232462)). The authors acknowledge Dr Enrico Anderlini for his valuable input in the PTO section.

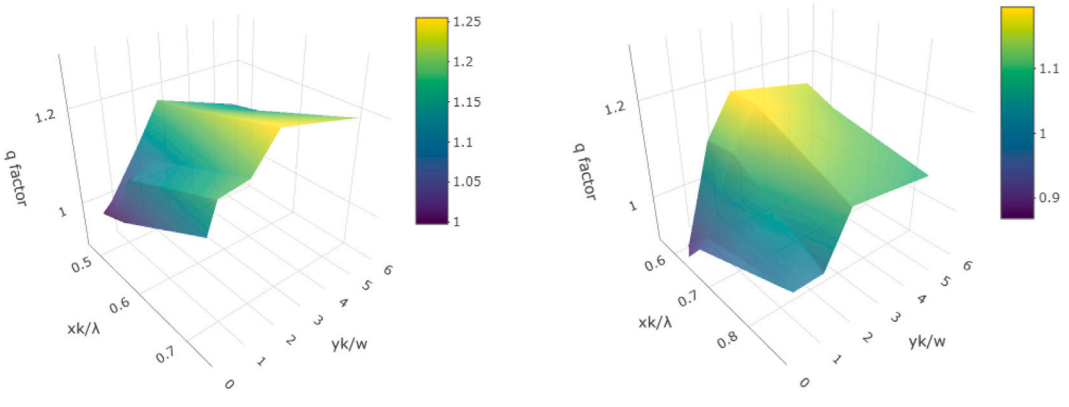

(a) $T_1 = 1.34$ s (b) $T_2 = 1.19$ s

(c) $T_3 = 1.03$ s

Fig. 18. Surface plots showing the variation of the q factor estimated for layout CG3 operating under different periods. The interaction factor is shown in terms of the non-dimensional distances x_k/λ and y_k/w.

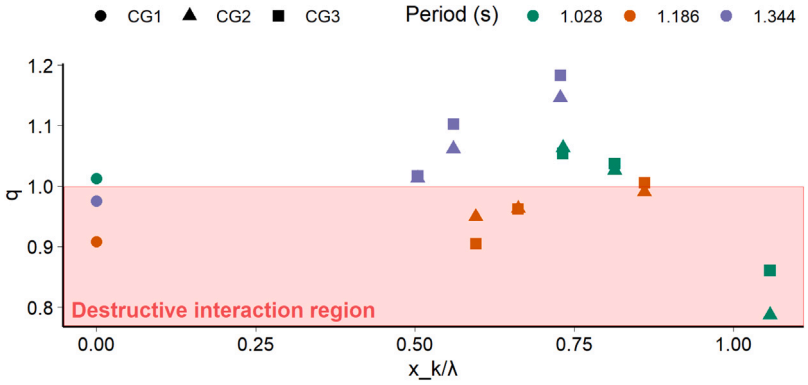

Fig. 19. Comparison of all the arrangements at different longitudinal spacings X_k and wave periods. The distance in the y-direction is 0.35 m.

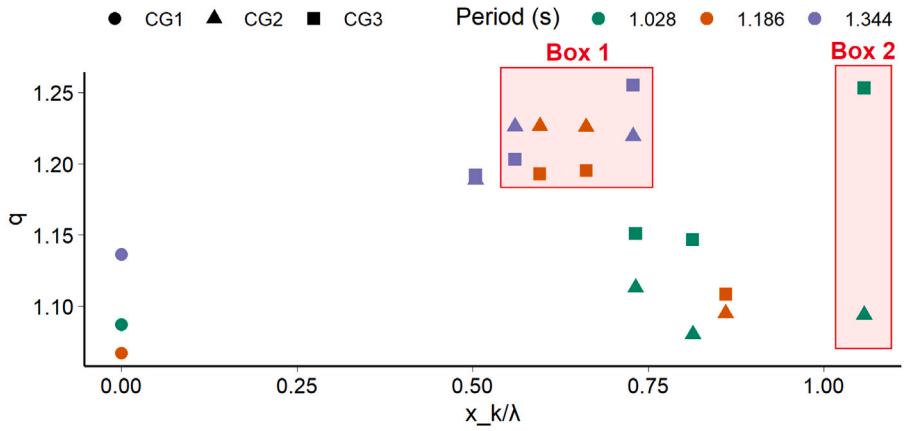

Fig. 20. Comparison of all the arrangements at different longitudinal spacings X_k and wave periods. The distance in the y-direction is 1.50 m.

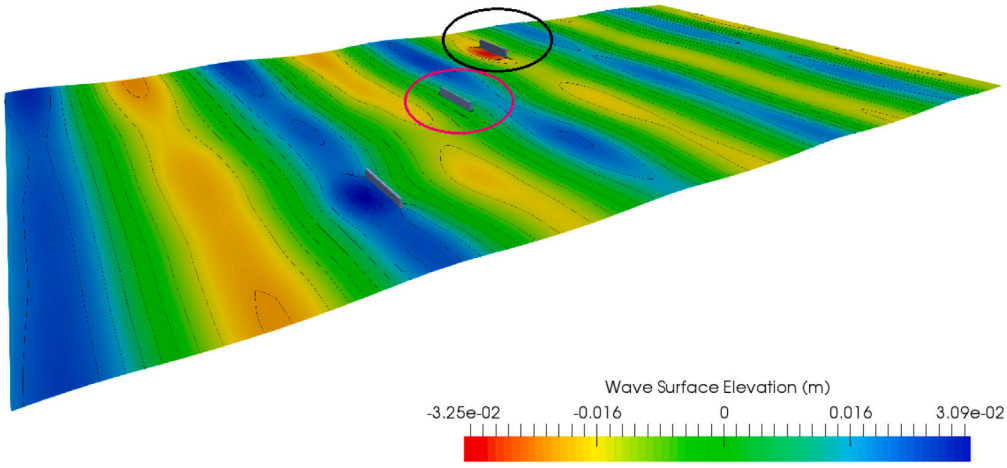

(a) Layout CG2

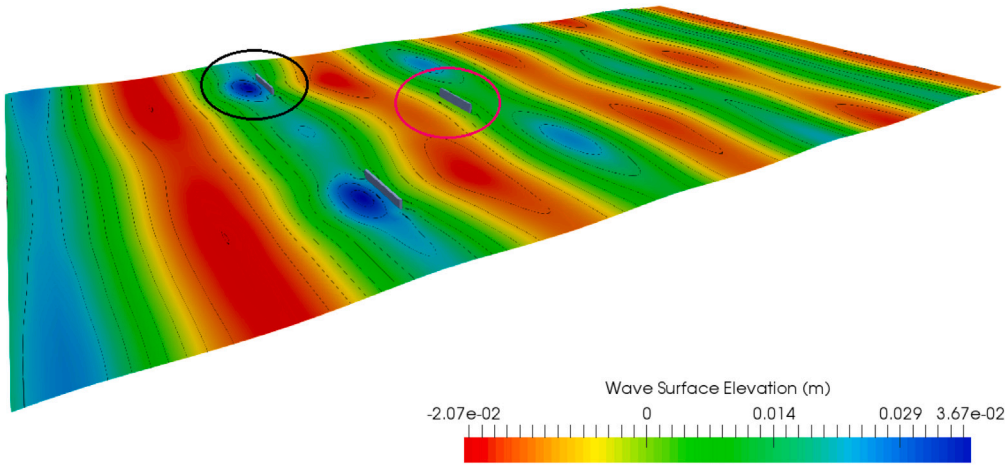

(b) Layout CG3

Fig. 21. Comparison of the wave surface elevation taken from the simulations of the staggered configurations at 17 s. In this setting, the longitudinal distance between the devices is X_3 = 1.56 m.

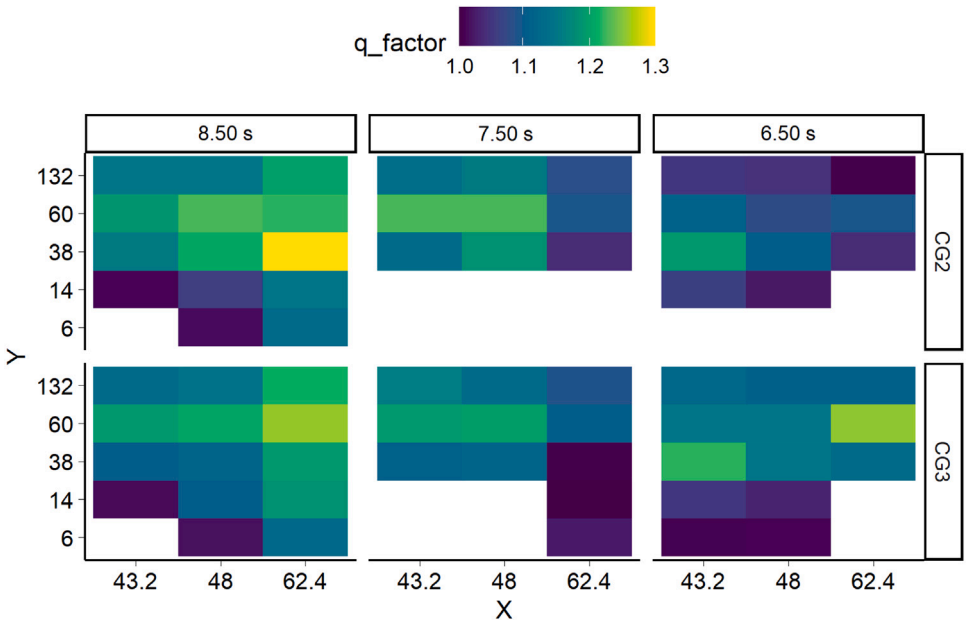

Fig. 22. Dimensional separating distances between the WECs that bring a positive interaction in terms of the q factor. The results are presented for both staggered configurations and the three periods considered.

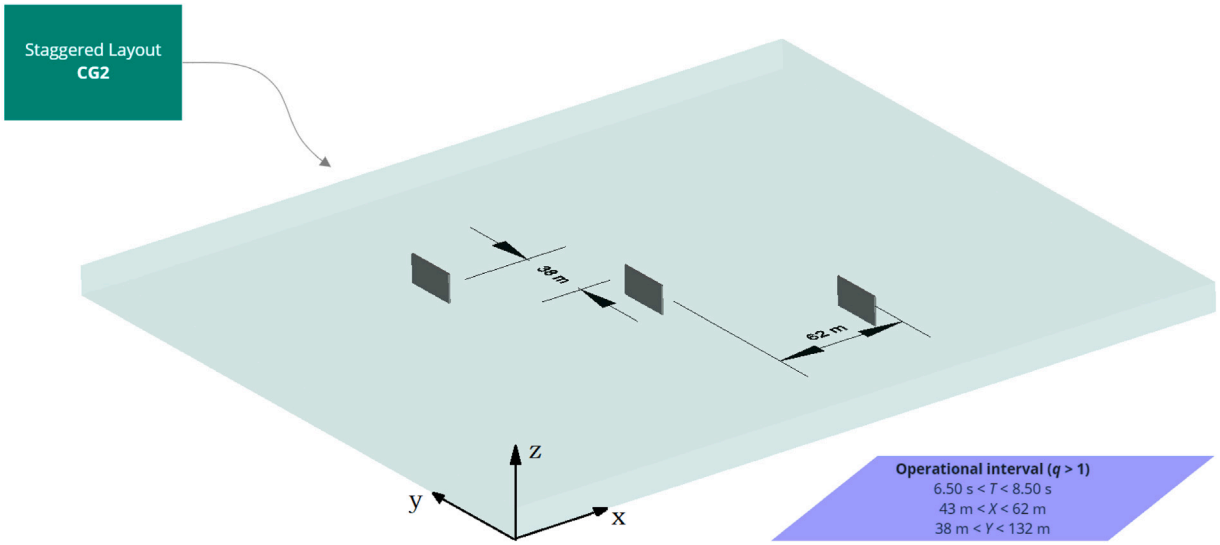

Fig. 23. Isometric view: Recommended layout for enhancing the power absorbed by a three-OWSC array. The improvement in the power capture under a set of operational parameters between 6.50 s $< T <$ 8.50 s is up to 30%.

References

[1] Danial Khojasteh, Abbas Shamsipour, Luofeng Huang, Sasan Tavakoli, Milad Haghani, Francois Flocard, Maryam Farzadkhoo, Gregorio Iglesias, Mark Hemer, Matthew Lewis, et al., A large-scale review of wave and tidal energy research over the last 20 years, Ocean Eng. 282 (2023) 114995.

[2] ITTC, Hydrodynamic Modelling of Marine Renewable Energy Devices - Final Report and Recommendations to the 29th ITTC, Technical Report, 2021.

[3] Jonathan Hodges, Jillian Henderson, Lauren Ruedy, Matthijs Soede, Jochem Weber, Pablo Ruiz-Minguela, Henry Jeffrey, Elva Bannon Bannon, Matthew Holland, Ruari Maciver, David Hume, José Luis Villate, Tim Ramsey, An International Evaluation and Guidance Framework for Ocean Energy Technology, IEA-OES, Technical Report, 2021, p. 68.

[4] Wenchuang Chen, Zhenhai Huang, Yongliang Zhang, Liguo Wang, Luofeng Huang, Hydrodynamic performance of a three-unit heave wave energy converter array under different arrangement, Renew. Energy 221 (2024) 119808.

[5] Aurélien Babarit, A database of capture width ratio of wave energy converters, Renew. Energy 80 (2015) 610–628.

[6] Aurélien Babarit, J. Hals, M.J. Muliawan, A. Kurniawan, T. Moan, J. Krokstad, Numerical benchmarking study of a selection of wave energy converters, Renew. Energy 41 (2012) 44–63.

[7] Emiliano Renzi, Frederic Dias, Hydrodynamics of the oscillating wave surge converter in the open ocean, Eur. J. Mech. B Fluids 41 (2013) 1–10.

[8] Siming Zheng, John Wilfrid Phillips, Martyn Hann, Deborah Greaves, Mathematical modelling of a floating clam-type wave energy converter, Renew. Energy 210 (2023) 280–294.

[9] Emiliano Renzi, Kenneth Doherty, Alan Henry, Frederic Dias, How does oyster work? The simple interpretation of oyster mathematics, Eur. J. Mech. B Fluids 47 (June 2012) (2014) 124–131.

[10] Emiliano Renzi, Frederic Dias, Relations for a periodic array of flap-type wave energy converters, Appl. Ocean Res. 39 (2013) 31–39.

[11] Imogen F. Noad, Richard Porter, Optimisation of arrays of flap-type oscillating wave surge converters, Appl. Ocean Res. 50 (2015) 237–253.

[12] Zhi Yung Tay, Vengatesan Venugopal, Hydrodynamic interactions of oscillating wave surge converters in an array under random sea state, Ocean Eng. 145 (August 2015) (2017) 382–394.

[13] E. Renzi, A. Abdolali, G. Bellotti, F. Dias, Wave-power absorption from a finite array of oscillating wave surge converters, Renew. Energy 63 (2014) 55–68.

[14] Dripta Sarkar, Emiliano Renzi, Frédéric Dias, Wave farm modelling of oscillating wave surge converters, Proceedings of the Royal Society A: Mathematical, Physical and Engineering Sciences 470 (2167) (2014) 20140118.
[15] Dripta Sarkar, Emile Contal, Nicolas Vayatis, Frederic Dias, Prediction and optimization of wave energy converter arrays using a machine learning approach, Renew. Energy 97 (2016) 504–517.
[16] L. Cameron, R. Doherty, Alan Henry, K. Doherty, J Van Hoff, D. Kaye, D. Naylor, S. Bourdier, Trevor Whittaker, Design of the next generation of the oyster wave energy converter, in: 3rd International Conference on Ocean Energy, (October), 2010, pp. 1–12.
[17] Ashkan Rafiee, Frederic Dias, Two-dimensional and three-dimensional simulation of wave interaction with an oscillating wave surge converter, in: International Workshop on Water Waves and Floating Bodies (IWWWFB), 2013.
[18] Moises Brito, R.B. Canelas, O. García-feal, J.M. Domínguez, A.J.C. Crespo, R.M.L. Ferreira, M.G. Neves, L. Teixeira, A numerical tool for modelling oscillating wave surge converter with nonlinear mechanical constraints, Renew. Energy 146 (2020) 2024–2043.
[19] Markel Penalba, Giussepe Giorgi, John V. Ringwood, Mathematical modelling of wave energy converters: A review of nonlinear approaches, Renew. Sustain. Energy Rev. 78 (May) (2017) 1188–1207.
[20] Daniela Benites Munoz, Luofeng Huang, Giles Thomas, The interaction of cnoidal waves with oscillating wave surge energy converters, in: The 14th OpenFOAM Workshop, 2019.
[21] Daniela Benites-Munoz, Luofeng Huang, Enrico Anderlini, José R Marín-Lopez, Giles Thomas, Hydrodynamic modelling of an oscillating wave surge converter including power take-off, J. Mar. Sci. Eng. 8 (10) (2020) 771.
[22] Daniela Benites-Munoz, Luofeng Huang, Enrico Anderlini, Jose Marín-López, Giles Thomas, Simulation of the wave evolution and power capture of an oscillating wave surge converter, in: ISOPE International Ocean and Polar Engineering Conference, ISOPE, 2020, pp. ISOPE–I.
[23] Luofeng Huang, Yuzhu Li, Daniela Benites-Munoz, Christian Windt Windt, Anna Feichtner, Sasan Tavakoli, Josh Davidson, Ruben Paredes, Tadea Quintuna, Edward Ransley, et al., A review on the modelling of wave-structure interactions based on OpenFOAM, OpenFOAM® J. 2 (2022) 116–142.
[24] Yanji Wei, Ashkan Rafiee, Alan Henry, Frédéric Dias, Wave interaction with an oscillating wave surge converter. Part I: Viscous effects, Ocean Eng. 113 (2016) 319–334.
[25] Pal Schmitt, Bjorn Elsaesser, The application of froude scaling to model tests of oscillating wave surge converters, Ocean Eng. 141 (June) (2017) 108–115.
[26] A tensorial approach to computational continuum mechanics using object-oriented techniques, Comput. Phys. 12 (6) (1998) 620–631.
[27] Hrvoje Jasak, OpenFOAM: Open source CFD in research and industry, Int. J. Nav. Archit. Ocean Eng. 1 (2) (2009) 89–94.
[28] Pal Schmitt, Bjorn Elsaesser, On the use of OpenFOAM to model oscillating wave surge converters, Ocean Eng. 108 (2015) 98–104.
[29] Pal Schmitt, Investigation of the Near Flow Field of Bottom Hinged Flap Type Wave Energy Converters (Ph.D. thesis), Queen's University Belfast, 2013.
[30] Robert G. Dean, Robert A. Dalrymple, Water Wave Mechanics for Engineers and Scientists, Vol. 2, World Scientific Publishing Company, 1991.
[31] Javier L Lara, Pablo Higuera, Raul Guanche, Inigo J Losada, Wave interaction with piled structures: Application with IH-FOAM, in: International Conference on Offshore Mechanics and Arctic Engineering, Vol. 55416, American Society of Mechanical Engineers, 2013, V007T08A078.
[32] Pablo Higuera, Enhancing active wave absorption in RANS models, Appl. Ocean Res. 94 (2020) 102000.
[33] Mart Borsboom, Niels G. Jacobsen, A generating-absorbing boundary condition for dispersive waves, Internat. J. Numer. Methods Fluids 93 (8) (2021) 2443–2467.
[34] Zhengyu Hu, Luofeng Huang, Yuzhu Li, Fully-coupled hydroelastic modeling of a deformable wall in waves, Coast. Eng. 179 (2023) 104245.
[35] F. Moukalled, L. Mangani, M. Darwish, The Finite Volume Method in Computational Fluid Dynamics, Vol. 113, Springer International Publishing, 2016, pp. 535–557.
[36] N.M. Newmark, A method of computation for structural dynamics, J. Eng. Mech. Divis. (1959).
[37] P.F. Pai, Highly Flexible Structures - Modeling, Computation, and Experimentation, American Institute of Aeronautics and Astronautics, 2007.
[38] H.A. Moossavi Buchholdt, S.E. Nejad, Response of linear and non-linear one degree-of-freedom systems to random loading : time domain analysis, in: Structural Dynamics for Engineers, second ed., 2012, pp. 117–135, chapter 6.
[39] M. Zonal, Two-equation kw turbulence models for aerodynamic flows, in: 24th Fluid Dynamics Conference, Orlando, FL, USA, 1993.
[40] Blanca Pena, Luofeng Huang, A review on the turbulence modelling strategy for ship hydrodynamic simulations, Ocean Eng. 241 (2021) 110082.
[41] Cyril W. Hirt, Billy D. Nichols, Volume of fluid (VOF) method for the dynamics of free boundaries, J. Comput. Phys. 39 (1) (1981) 201–225.
[42] Henk Kaarle Versteeg, Weeratunge Malalasekera, An Introduction to Computational Fluid Dynamics: The Finite Volume Method, Pearson Education, 2007.
[43] Luofeng Huang, Sasan Tavakoli, Minghao Li, Azam Dolatshah, Blanca Pena, Boyin Ding, Abbas Dashtimanesh, CFD analyses on the water entry process of a freefall lifeboat, Ocean Eng. 232 (2021) 109115.
[44] Luofeng Huang, Fang Li, Minghao Li, Danial Khojasteh, Zhenhua Luo, Pentti Kujala, An investigation on the speed dependence of ice resistance using an advanced CFD+ DEM approach based on pre-sawn ice tests, Ocean Eng. 264 (2022) 112530.
[45] ITTC-Recommended Procedures, Guidelines: Practical guidelines for ship CFD applications, ITTC Rep. 7 (2014) 2–18.
[46] Louise O'Boyle, Kenneth Doherty, Jos van 't Hoff, Jessica Skelton, The value of full scale prototype data - testing oyster 800 at EMEC, Orkney, in: Proceedings of the 11th European Wave and Tidal Energy Conference, 2015, pp. 1–10.
[47] Umesh A. Korde, John Ringwood, Hydrodynamic control of wave energy devices, 2016, pp. 1–381.
[48] Johannes Falnes, Ocean Waves and Oscillating Systems, Cambridge University Press, 2002.
[49] Markel Penalba, Josh Davidson, Christian Windt, John V. Ringwood, A high-fidelity wave-to-wire simulation platform for wave energy converters: Coupled numerical wave tank and power take-off models, Appl. Energy 226 (May) (2018) 655–669.
[50] Aleix Maria-Arenas, Aitor J. Garrido, Eugen Rusu, Izaskun Garrido, Control strategies applied to wave energy converters: State of the art, Energies 12 (16) (2019).
[51] Enrico Anderlini, Control of Wave Energy Converters Using Machine Learning Strategies (Ph.D. thesis), Universities of Edinburgh, Exeter and Strathclyde, 2017, p. 255.
[52] Johannes Falnes, Ocean waves and oscillating systems, 2020.
[53] Rui P.F. Gomes, Miguel F.P. Lopes, João C.C. Henriques, Luís M.C. Gato, António F. de O. Falcão, The dynamics and power extraction of bottom-hinged plate wave energy converters in regular and irregular waves, Ocean Eng. 96 (2015) 86–99.
[54] Kjell Budal, Theory for absorption of wave power by a system of interacting bodies, J. Ship Res. 21 (4) (1977).
[55] João Cruz, Ocean Wave Energy, Springer-Verlag, 2008, p. 435.
[56] Hamed Behzad, P. Sanaei, On optimizing the wave energy converters configuration in a farm, 1 (1) (2019) 1–14.